https://dx.doi.org/10.21577/0103-5053.20200080

J. Braz. Chem. Soc., Vol. 31, No. 11, 2282-2298, 2020
Printed in Brazil - ©2020 Sociedade Brasileira de Química

Article

Synthesis, Characterization, Spectroelectrochemical, Photophysical and HSA-Binding Properties of Novel and Versatile *meso*-Tetra(4-pyridylvinylphenyl)porphyrins Coordinated to Ruthenium(II)-Polypyridyl Derivatives

Viviane Viecelli,[a] Otávio A. Chaves,[b] Koiti Araki,[c] Paulo R. Martins[,d] and Bernardo A. Iglesias*[,a]*

[a]*Laboratório de Bioinorgânica e Materiais Porfirínicos, Departamento de Química, Universidade Federal de Santa Maria, Av. Roraima 1000, 97105-900 Santa Maria-RS, Brazil*

[b]*Instituto SENAI de Inovação em Química Verde, Rua Morais e Silva 53, 20271-030 Rio de Janeiro-RJ, Brazil*

[c]*Instituto de Química, Universidade de São Paulo, Av. Prof Lineu Prestes 748, 05508-000 São Paulo-SP, Brazil*

[d]*Instituto de Química, Universidade Federal de Goiás, Av. Esperança s/n, 74690-900 Goiânia-GO, Brazil*

The free-base *meso*-tetra(4-pyridylvinylphenyl)porphyrin (**1a**) and its zinc(II) complex were synthesized and then functionalized with $[Ru(bpy)_2Cl]^+$ units (**2a** and **2b**) via conventional methods and evaluated in terms of photophysical, electrochemical and biological aspects. All porphyrins present moderate singlet oxygen production and fluorescence quantum yield, and did not show any aggregation process. The photo-oxidation ability of those porphyrins decreased in the order **2b** > **1a** > **2a**. The electrochemical behavior of **2a** and **2b** modified electrodes was evaluated by electroanalytical methods. Also the **2b** electrode showed a smaller charge transfer resistance (36.70 Ω) when compared to **2a** electrode (45.17 Ω). In addition, even after 30 consecutive injections of nitrite solution (1.0×10^{-4} mol L^{-1}) using the flow injection analysis (FIA) system, the modified **2b** electrode showed an relative standard deviation (RSD, n = 30) of 1.36% exhibiting a great potential as amperometric sensor for nitrite. Moreover, the biological evaluation towards human serum albumin (HSA) indicated spontaneous, weak and ground-state association in the IB subdomain (site III) and possibly a second site, changing the conventional interaction mode of porphyrins with biomolecules as consequence of the longer arms (porphyrin ring substituents at *meso*-positions) ending with a ruthenium polypyridyl complex, that may enhance the photodynamic therapy (PDT) efficiency of photogenerated reactive oxygen species (ROS) species.

Keywords: porphyrins, ruthenium(II) complexes, electrocatalysis, singlet oxygen, HSA-binding

Introduction

Porphyrins and metalloporphyrins have been extensively explored in many fields, including biology,[1] medicine,[2] supramolecular chemistry,[3] and materials/nanomaterials science,[4] mainly due to their catalytic/electrocatalytic,[5] photochemical and photophysical properties,[6] which are strongly dependent on the metal ion coordinated to the macrocyclic ring, as well as on its oxidation state and axial ligands. In addition, several functional groups can be appended to the *meso*- and/or β-pyrrole carbons in order to generate convenient building-blocks for supramolecular systems based on electrostatic, hydrogen bonding, π-π or hydrophobic interactions, or on coordination chemistry-based approach using suitable transition metal ion complexes.[7] The last one is particularly interesting because it allows the preparation of supramolecular porphyrin systems encompassing redox and/or photochemically active peripheral groups, providing versatile interaction sites for biomolecules,[8] and as electron or energy transfer relays.[9]

*e-mail: pauloqmc@ufg.br; bernardopgq@gmail.com, bernardo.iglesias@ufsm.br

Dedicated to Professor Henrique Eisi Toma on the occasion of his 70th birthday.

For instance, *meso*-tetra(pyridyl)porphyrins have been used as multi-bridging units to form highly organized multinuclear species with $[Ru(bpy)_2Cl]^+$, $[Ru(phen)_2Cl]^+$, $[Ru(edta)]^-$ or $[Ru(NH_3)_5]^{2+}$ complexes (bpy: 2,2'-bipyridine; phen: 1,10-phenanthroline; edta: ethylenediamine tetraacetic acid), exhibiting enhanced electrocatalytic and photoelectrochemical properties. Araki, Toma and co-workers[10-12] described *meso*-tetra(4-pyridyl) porphyrins bound to four peripheral $[Ru(bpy)_2Cl]^+$ moieties as interesting building-blocks of electrochemically active homogeneous films that can be employed in amperometric sensors for analyses of several chemical and biological reducing species.

Moreover, the peripheral transition metal complexes can be used to modulate the properties of the metalloporphyrin core by induced electronic and steric effects.[13] Thus, the properties of supramolecular porphyrins are strongly dependent on the electronic coupling between the central and peripheral groups, such that the use of molecular bridges exhibiting possible isomerization or photo-isomerization reactions can give rise to interesting molecular switches.[14] Among the functional species that can be used for such a purpose, vinyl-pyridyl units are particularly interesting because of their well-known photoinduced *cis-trans* isomerization reaction.[15]

Human serum albumin (HSA) is considered as the main globular protein in the human bloodstream, playing different roles in many biological processes.[16] HSA is the major soluble protein in the human circulatory system, responsible for transporting and disposing various endogenous and exogenous compounds,[17] generally those more hydrophobic and poorly soluble in water. In general, information on non-covalent binding of tetrapyrrolic macrocycle to HSA is acquired by spectroscopic methods, as previously reported in the literature.[18-20]

Based on the background described above on the wide scientific importance of *meso*-tetra(pyridyl)porphyrin derivatives, the present article describes the synthesis of a new free-base *meso*-tetra(4-pyridylvinylphenyl)porphyrin (**1a**) and its functionalization with $[Ru(bpy)_2Cl]^+$ units, to form the *meso*-tetra-ruthenated(4-pyridylvinylphenyl) porphyrin (**2a**) and its respective zinc(II) complex (**2b**) (Figure 1). All compounds were evaluated by structural, spectroscopic and electrochemical analysis. Moreover, their photostability, singlet oxygen production and preliminary effects on HSA-binding were evaluated by UV-Vis absorption and steady-state fluorescence emission spectroscopy, as well as molecular docking calculation.

Experimental

General: materials and methods

All reagents and solvents were analytical grade and they were purchased from Sigma-Aldrich®, St. Louis, MO, USA or local suppliers. Column chromatography was carried out using silica-flash 230-400 mesh from Sigma-Aldrich®, St. Louis, MO, USA. Analytical preparative thin-layer chromatography (TLC) was performed using Merck, St. Louis, MO, USA, TLC silica-gel 60 F_{254} plates on

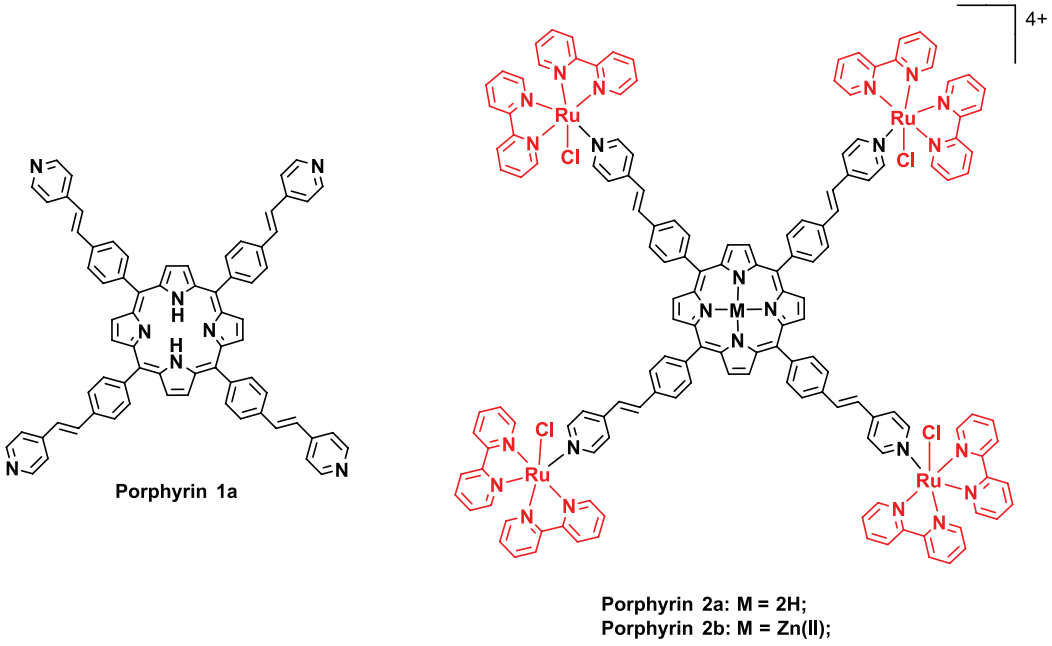

Figure 1. Chemical structure for the porphyrins **1a**, **2a**, and **2b**. In the case of porphyrins **2a** and **2b**, the trifluoromethanesulfonate anions were omitted for clarity.

aluminum sheets (1.0 mm thick). The $[Ru(bpy)_2Cl_2]\cdot 3H_2O$ complex was prepared refluxing $RuCl_3\cdot nH_2O$ with 2,2'-bipyridine and LiCl in *N*,*N*-dimethylformamide (DMF), as previously described by Meyer and co-workers.[21]

Elemental analyses CHN% were performed using a PerkinElmer CHN 2400 microanalysis instrument. Mass spectra by electrospray ionization (ESI-(+)-MS) were aquired in a Bruker Daltonics Esquire 3000 Plus equipment using the following conditions: capillary voltage 3.0 kV, sample cone 30 V, extraction cone 3.0 V, source temperature 100 °C, desolvation temperature 100 °C in N_2 gas with flow rate of 400 mL min^{-1}. The ^1H nuclear magnetic resonance (NMR) and correlation spectroscopy (COSY) 2D spectra of the porphyrins were obtained on a Bruker APX300 and DRX500 spectrophotometers using deuterated dimethyl sulfoxide (DMSO-d_6) and acetonitrile (CD_3CN) as solvents, and tetramethylsilane (TMS) as internal reference. The chemical shifts (δ) were expressed in ppm and coupling constants (J) were given in hertz (Hz).

Absorption and luminescence methods

Electronic absorption spectra were recorded on a Shimadzu model UV2600 diode array spectrophotometer. Steady-state fluorescence emission spectra were collected using a Varian Cary50 instrument (slit 2.0 mm; for both emission and excitation channel). Fluorescence quantum yields (Φ_F) of the porphyrins **1a**, **2a** and **2b** in dichloromethane (DCM) or acetonitrile (CH_3CN) solutions were determined by comparing the corrected fluorescence spectra with that of *meso*-tetra(phenyl)porphyrin (TPP) in dichloromethane ($\Phi_F = 0.15$) as standard.[22] The fluorescence spectra of the samples and the standard were collected in the same experimental conditions, and the fluorescence quantum yield was calculated by using equation 1:

$$\Phi_F = \Phi_{Fstd} \frac{I}{I_{std}} \frac{\left(1-10^{-A}\right)_{std}}{\left(1-10^{-A}\right)} \frac{\eta}{\eta_{std}} \quad (1)$$

where Φ_F, I, A and η are the fluorescence quantum yield, the integrated area of the emission band, the absorbance in the excitation wavelength (λ_{exc}) and refractive index of the solvent, respectively. The subscript "std" refers to the TPP used as fluorescence standard.

Electrochemical and spectroelectrochemical analysis

Cyclic voltammetry measurements were carried out using an Autolab PGSTAT 30 potentiostat/galvanostat using a conventional three electrodes system constituted by a glassy carbon working electrode, a platinum wire as auxiliary, and an Ag/Ag^+ (0.01 mol L^{-1} in acetonitrile) as reference electrode. The experiments were carried out using 0.1 mol L^{-1} of tetra-butyl-ammonium perchlorate salt ($TBAClO_4$) in dry DMF as support electrolyte.

The spectroelectrochemistry data were collected using a previously described[23] homemade thin-layer cell, a PAR model 283 potentiostat/galvanostat and the HP-8453A spectrophotometer.

Preparation of thin films of porphyrins **2a** and **2b**

Thin films of porphyrins **2a** and **2b** were prepared according to the following procedure: a glassy carbon electrode was previously polished with alumina slurry (1.0 μm), rinsed copiously with water, and modified using a porphyrin solution. Typically, 50 μL of a methanolic solution of each porphyrin (1×10^{-4} mol L^{-1}) was transferred to the electrode surface and allowed to dry in air. A typical volume of 50 μL is perfect for covering the whole glassy carbon electrode surface.

The cyclic voltammetric and electrochemical impedance spectroscopy measurements were performed in an Ecochemie PGSTAT 30 potentiostat/galvanostat, using a conventional three electrodes system consisting of a porphyrin modified glassy carbon as working electrode, a reference electrode (Ag/AgCl (KCl, 1.0 mol L^{-1})) and a platinum wire as auxiliary electrode. The cyclic voltammograms were obtained in the absence and presence of nitrite solution (9.9×10^{-5} to 1.1×10^{-3} mol L^{-1}) in the range of +0.22 to +1.22 V, at a scan rate of 100 mV s^{-1}, in 0.1 mol L^{-1} nitric acid (HNO_3) solution. The electrochemical impedance spectroscopy was performed at +1.0 V *vs.* standard hydrogen electrode (SHE) using a perturbation amplitude of ± 10 mV and frequency range of 100 kHz to 0.1 Hz. The analytical repeatability of electrodes modified with **2b** was evaluated under hydrodynamic conditions in a flow injection analysis (FIA) system (see Supplementary Information (SI) section).

The potentials measured in DMF were converted to SHE by adding +0.503 V, whereas the potentials in aqueous solution obtained using the Ag/AgCl (1.0 mol L^{-1} KCl) reference electrode was converted to SHE by adding +0.222 V.

Photostability and singlet oxygen generation assays

The photostability of *meso*-tetra-substituted porphyrins **1a**, **2a** and **2b** at concentrations in the 1.0 to 2.0 μM range in DMSO solution was determined by measuring the absorbance at Soret band before and after irradiation with white light-emitting diode (LED)

array system for 60 min (visible region), at irradiance of 25 mW cm^{-2} and fluence rate of 90 J cm^{-2}. All experiments were performed independently in duplicate.

For the determination of singlet oxygen generation, solutions containing 20 μM of the $^1O_2$ scavenger 1,3-diphenylisobenzofuran (DPBF),[24] in the presence and absence of each porphyrin derivative in the concentration of 0.5 μM, were prepared in DMF solution and transferred into a 1.0 × 1.0 cm quartz cuvette. The solutions were irradiated during 180 s, at room temperature, under a gentle magnetic stirring, using 660 nm diode laser positioned at 2.0 cm from the sample (TheraLase DMC, São Carlos, SP, Brazil), setting the power to 100 mW, while monitoring the decrease in absorbance at 415 nm (oxidation of DBPF scavenger).

Singlet oxygen quantum yield measurement

In a typical experiment of DPBF photo-degradation,[25] 2.5 mL of 100 μM DPBF in DMSO solution was mixed with 0.5 mL (ca. 20 μM) of porphyrin. In order to measure $^1O_2$ generation, absorption spectra of the solutions (samples and standard) were recorded for different exposure times by using a 660 nm diode laser positioned 2.0 cm from the sample (TheraLase DMC, São Carlos, SP, Brazil) with an average power of 100 mW, during 180 s. The singlet oxygen production quantum yield (Φ_Δ) was calculated by using equation 2:

$$\Phi_\Delta = \Phi_\Delta^{std} \frac{k}{k^{std}} \frac{I^{std}}{I} \quad (2)$$

in which, $I^{std} / I = (1 - 10^{A std}) / (1 - 10^{A})$, Φ_Δ^{std} is the singlet oxygen quantum yield of standard sample (in our case, TPP dissolved in DMF, $\Phi_\Delta^{std} = 0.66$),[26,27] k and k^{std} are the photo-degradation kinetic constants for porphyrins **1a**, **2a** and **2b** and TPP (standard), respectively, and A^{std} and A are the absorbances of TPP and porphyrins **1a**, **2a** and **2b** solutions, respectively.

HSA-binding assays by steady-state fluorescence emission

The interaction of HSA with the porphyrins **1a**, **2a** and **2b** was studied by steady-state fluorescence emission at room temperature in a Tris-HCl buffer solution (pH = 7.4). A stock solution (10^{-6} mol L^{-1} range) was prepared in DMSO and successive aliquots of each porphyrin were added into the HSA solution (15 μM) in order to get concentrations ranging from 0 to 150 μM. The samples were excited at 290 nm and the fluorescence emission evaluated in the range of 300 to 550 nm. The inner filter effect of each porphyrin was considered in the HSA-binding assays. Generally, fluorescence quenching can occur by static or dynamic mechanisms, and the fluorescence quenching experiments data analyzed using the Stern-Volmer equation 3.

$$\frac{F_0}{F} = 1 + k_q \tau_0 [Q] = 1 + K_{SV} [Q] \quad (3)$$

where F_0 and F are the fluorescence intensities in the absence and presence of the quencher, whereas K_{SV}, k_q, τ_0 and [Q] denote the Stern-Volmer constant, the bimolecular quenching rate constant, the fluorescence lifetime of HSA (5.67×10^{-9} s)[28] and the concentration of quencher, respectively. According to equation 3, the Stern-Volmer constant (K_{SV}) was calculated from the slope and k_q is equal to K_{SV} / τ_0.

For static fluorescence quenching mechanism, it is expected lower k_q values with increasing temperatures since the stability of the complex tend to decrease whilst the opposite effect is expected for the dynamic fluorescence quenching mechanism.[20] Diffusion-controlled quenching typically results in values of k_{diff} ca. 7.40×10^9 M^{-1} s^{-1}, according to Smoluchowski-Stokes-Einstein theory at 298 K, which is considered to be the highest possible value in aqueous solution for macromolecules.[29] Smaller k_q values can result from steric shielding of the porphyrins, and larger apparent k_q values usually indicate some type of binding interaction.

In order to estimate the association constant value (K_a) and the number of binding sites (n) the double logarithmic approximation was applied, as represented by equation 4:

$$\log\left(\frac{F_0 - F}{F}\right) = \log K_a + n \log [Q] \quad (4)$$

where F_0 and F represent fluorescence intensities in the absence and presence of the quencher, respectively, and [Q] the concentration of the porphyrin. According to equation 4, the K_a value can be calculated from the intercept (linear coefficient) of the plot, while n value is given by the slope.

The standard Gibbs free-energy (ΔG^o) of porphyrin-HSA adducts was calculated from the values of K_a using the equation 5:

$$\Delta G^o = -RT \ln K_a \quad (5)$$

where R and T are the gas constant (1.987 kcal K^{-1} mol^{-1}) and the temperature (298 K), respectively.

Molecular docking analysis with HSA

The crystallographic structure of HSA was obtained from

Protein Data Bank (access code: 1N5U).[30] The chemical structure of the porphyrins **1a**, **2a** and **2b** were built and the energy minimized by density functional theory (DFT) using the Spartan'14 software.[31] The molecular docking calculation for the porphyrins in the protein model was performed with GOLD 5.7 software.[32] Hydrogen atoms were added to the protein considering the tautomeric states and ionization data, which are inferred by the GOLD 5.7 software.

The HSA structure presents three main binding pockets which were explored in the theoretical calculations (subdomains IIA, IIIA and IB).[33,34] The number of genetic operations (crossing, migration, mutation) during the search procedure was set as 100,000. The program optimizes the geometry for hydrogen bonding by allowing the rotation of hydroxyl and amino groups of the amino acid chain. In addition, due to the high volume of each porphyrin under study, some amino acid residues stayed flexible during the docking runs. The side chain rotamers have been defined according to the availability of the library. The default function of GOLD 5.7 software[32] ChemPLP was used as scoring function. The figures of the best docking pose were generated with PyMOL Delano Scientific LLC program.[35]

Preparation of free-base porphyrin **1a**

The free-base porphyrin **1a** was prepared according to modified Adler methodology[36] (Scheme 1), by direct cyclization reaction of 4-(4-pyridylvinyl)benzaldehyde[37] (1.00 g; 4.77 mmol; 1.0 equiv.) and pyrrole (0.34 mL; 4.77 mmol; 1.0 equiv.) in refluxing propionic acid (100 mL) during 90 min. In the next step, the solvent was removed, and the purple color porphyrin was precipitated out by addition of ethanol. The porphyrin **1a** was purified by silica-gel column chromatography using DCM/MeOH (90:10; v/v) as eluent, and final recrystallization in DCM/*n*-hexane (1:5; v/v).

Spectroscopic data for *meso*-tetra(4-pyridylvinylphenyl) porphyrin (**1a**)

Yield: 0.230 g (0.223 mmol, 4.6%); λ (CH_3CN) / nm (ε / M^{-1} cm^{-1}) 369 (22,595), 417 (303,175), 512 (16,250), 546 (5,110), 587 (5,190), 643 (2,155); ^{1}H NMR (500 MHz, DMSO-d_6) δ 8.92 (d, 8H, *J* 5.0 Hz, H_a, *o*-Py), 8.87 (s, 8H, β-H), 8.69 (d, 8H, *J* 5.0 Hz, H_b, *m*-Py), 8.29 (d, 8H, *J* 15.0 Hz, H_{c-d}, vinyl-H), 8.18 (d, 8H, *J* 5.0 Hz, H_e, Ph), 8.15 (d, 8H, *J* 5.0 Hz, H_f, Ph), −2.95 (s, 2H, inner NH); ESI-MS *m/z*, calcd. for $C_{72}H_{50}N_8.4H_2O$ $[M]^+$: 1027.24, found: 1027.60; anal. calcd. for $C_{72}H_{50}N_8{\cdot}4H_2O$: C, 78.67; H, 5.32; N, 10.19%; found: C, 78.97; H, 5.34; N, 10.23%.

Preparation of tetra-ruthenated free-base porphyrin **2a** and zinc(II) complex **2b**

Free-base *meso*-tetra-ruthenated porphyrin **2a** was obtained according to modified Araki and co-workers[38] methodology (Scheme 2), by the direct reaction of *meso*-tetra(4-pyridylvinylphenyl)porphyrin **1a** (0.050 g; 0.048 mmol; 1.0 equiv.) and *cis*-[$Ru(bpy)_2Cl_2$] (0.096 g; 0.197 mmol; 4.05 equiv.), in the presence of glacial acetic acid (10 mL) as solvent, under reflux during 90 min. The solvent was evaporated, and crude material was dissolved in 1.0 mL of DMF, precipitated with saturated $LiCF_3SO_3$ aqueous solution, and filtered out using a sintered glass filter. Then, the precipitate was washed three times with distilled water and diethyl ether and dried overnight under vacuum to obtain the purified free-base tetra-ruthenated porphyrin **2a** as a red-brown solid.

Spectroscopic data of free-base *meso*-tetra-ruthenated (4-pyridylvinylphenyl)porphyrin (**2a**)

Yield: 0.035 g (0.039 mmol, 81%); λ (CH_3CN) / nm (ε / M^{-1} cm^{-1}) 294 (167,00), 416 (214,425), 512 (42,000), 555 (19,840), 592 (11,600), 647 (5,250); ^{1}H NMR (500 MHz, CD_3CN) δ 10.02 (m, 4H, 12,12',8,8'), 8.88

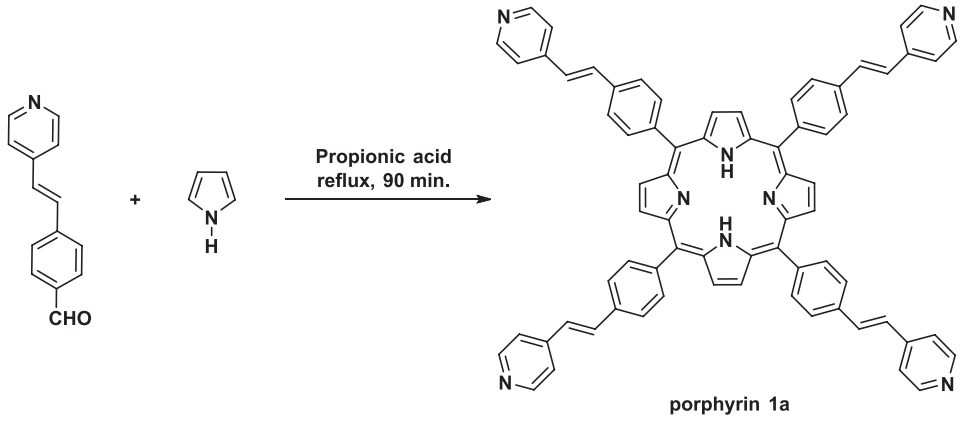

Scheme 1. Synthetic pathway for *meso*-tetra(4-pyridylvinylphenyl)porphyrin **1a**.

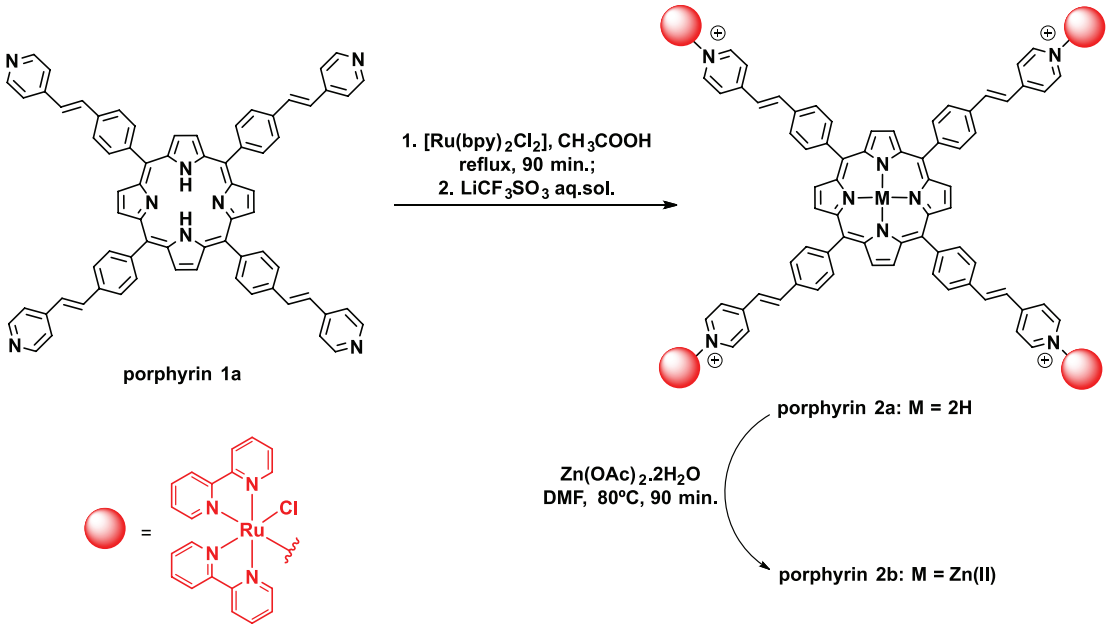

Scheme 2. Scheme showing the synthetic pathway for preparation of the tetra-ruthenated porphyrin **2a** and its respective zinc(II) complex **2b**.

(broad s, 8H, 2), 8.68 (d, 8H, *J* 5.5 Hz, 7), 8.40 (d, 4H, *J* 16.5 Hz, 5'), 8.24 (m, 8H, 11,11',15,15'), 8.02 (d, 8H, *J* 6.5 Hz, 3), 7.91 (d, 8H, *J* 5.5 Hz, 6), 7.86 (m, 4H, 14,14'), 7.84 (m, 4H, 10,10'), 7.50 (d, 8H, *J* 5.5 Hz, 4), 7.45 (d, 4H, *J* 16.5 Hz, 5), 7.26 (dd, 4H, *J* 7.0 Hz, 13,13'), 7.20 (dd, 4H, *J* 7.0 Hz, 9,9'), –2.84 (s, 2H, inner NH); anal. calcd. for $Ru_4C_{156}H_{130}N_{24}O_{20}F_{12}Cl_4S_4{\cdot}8H_2O$: C, 52.59; H, 3.68; N, 9.43%; found: C, 52.94; H, 3.71; N, 9.46%.

The zinc(II)-porphyrin derivative **2b** was obtained by reacting the free-base ruthenated porphyrin **2a** (0.030 g; 0.0087 mmol; 1.0 equiv.) with an excess of zinc(II) acetate dihydrate (0.010 g; 0.044 mmol; 5.0 equiv.), in the presence of DMF (5 mL) at 80 °C for 2 h. The solvent was evaporated out and the crude dark-brown solid washed with several amounts of diethyl ether, filtered and dried overnight under vacuum to get the purified zinc(II) tetra-ruthenated porphyrin **2b** complex.

Spectroscopic data of zinc(II) *meso*-tetra-ruthenated (4-pyridylvinylphenyl)porphyrin (**2b**)

Yield: 0.028 g (0.0082 mmol, 94%); λ (CH_3CN) / nm (ε / M^{-1} cm^{-1}) 293 (141,510), 427 (218,580), 560 (24,725), 602 (12,060); ^{1}H NMR (500 MHz, CD_3CN) δ 9.99 (m, 4H, 12,12',8,8'), 8.85 (broad s, 8H, 2), 8.65 (d, 8H, *J* 5.5 Hz, 7), 8.38 (d, 4H, *J* 16.5 Hz, 5'), 8.20 (m, 8H, 11,11',15,15'), 8.00 (d, 8H, *J* 6.5 Hz, 3), 7.88 (d, 8H, *J* 5.5 Hz, 6), 7.82 (m, 4H, 14,14'), 7.80 (m, 4H, 10,10'), 7.47 (d, 8H, *J* 5.5 Hz, 4), 7.39 (d, 4H, *J* 16.5 Hz, 5), 7.22 (dd, 4H, *J* 7.0 Hz, 13,13'), 7.18 (dd, 4H, *J* 7.0 Hz, 9,9'); anal. calcd. for $ZnRu_4C_{156}H_{132}N_{24}O_{22}F_{12}Cl_4S_4{\cdot}10H_2O$: C, 51.16; H, 3.63; N, 9.18%; found: C, 51.20; H, 3.66; N, 9.22%.

Results and Discussion

Synthesis of *meso*-tetra(4-pyridylvinylphenyl)porphyrins **2a** and **2b**

The free-base porphyrin containing four vinyl-pyridyl moieties was synthesized by reaction of the appropriate aldehyde and pyrrole in refluxing propionic acid. An equimolar stoichiometry of aldehyde and pyrrole was chosen to maximize the yield of the desired porphyrin (Scheme 1). The polymeric by-products of the reaction were removed and the resulting purple-bright powder purified by silica column chromatography using DCM:MeOH mixture as eluent to obtain the *meso*-tetra(4-pyridylvinylphenyl) porphyrin **1a**.

Considering the remarkable structural/spectroscopic properties of porphyrins and excellent binding features of ruthenium(II) polypyridyl moieties with biomolecules,[39] new supramolecular species combining those properties was envisaged and performed in a simple way by binding $[Ru(bpy)_2Cl]^+$ to the periphery of the porphyrin ring. The novel compounds were synthesized via post-modification of tetra-substituted (pyridylvinylphenyl)porphyrin **1a** with four equivalents of $[Ru(bpy)_2Cl]^+$ units. The reaction was carried out in glacial acetic acid (CH_3COOH) with a little excess of *cis*-dichloro(2,2'-bipyridine)ruthenium(II) *per* pyridyl group, at 120 °C, for 90 min (Scheme 2). Importantly, the presence of the positively charged peripheral ruthenium(II)-complexes in the porphyrin structure caused a significant increase in its solubility in organic solvents such as CH_3CN, DMSO and MeOH,

whereas the starting free-base porphyrin, **1a**, presents much lower solubility and strong tendency to aggregation.

Porphyrins **1a**, **2a** and **2b** were fully characterized by CHN%, ESI-MS, UV-Vis and NMR spectroscopy. The ^{1}H NMR spectrum of the free-base porphyrins **1a** and **2a** showed the inner ring protons resonance at high fields (−2.84 to −2.95 ppm range), while all other proton signals corresponding to the porphyrin peripheral groups were found in lower field regions. In the case of 4-pyridyl(vinyl) phenyl proton peaks, the resonances appeared as multiplets at δ 8.92-7.91 range, the *ortho* and *meta*-pyridyl protons relative to vinyl-H at δ 8.29-7.45 range, and the phenyl protons at δ 8.18-7.50 range. In all cases the porphyrin ring β-H protons were observed at δ 8.88. On the other hand, the multiplet resonances around δ 10.02, 8.24, 7.86, 7.84 and 7.20 were attributed to the $[Ru(bpy)_2Cl]^+$ moieties. The ^{1}H NMR spectrum of porphyrin **2b** shows the disappearance of the high field resonance when metallated with the zinc(II) ion, whereas the same spectral profile was observed for the proton resonances of the pyridyl(vinyl) phenyl groups and $[Ru(bpy)_2Cl]^+$ complexes, as expected. All collected NMR spectra and COSY 2D analyses data are listed in the Supplementary Information (SI) section (see Figures S1-S8).

Electronic absorption properties

Porphyrin **1a** was isolated as purple solid and its absorption spectra in the ultraviolet-visible range was typical of a free-base porphyrin structure, exhibiting the Soret and Q bands at 417, 512, 546, 587 and 643 nm in acetonitrile solution. The weak absorption peak of the pyridyl-vinyl units was observed at 369 nm, followed by the intense Soret band and Q transitions in the visible region (see Figure S2, SI section). The tetra-ruthenated porphyrin **2a** exhibited absorption bands at 416 nm (Soret band), 510 nm ($Q_{y(0-1)}$), 555 nm ($Q_{y(0-0)}$), 592 nm ($Q_{x(0-1)}$) and 647 nm ($Q_{x(0-0)}$), characteristic of the macrocycle ring, whereas the typical bipyridine intraligand transition band

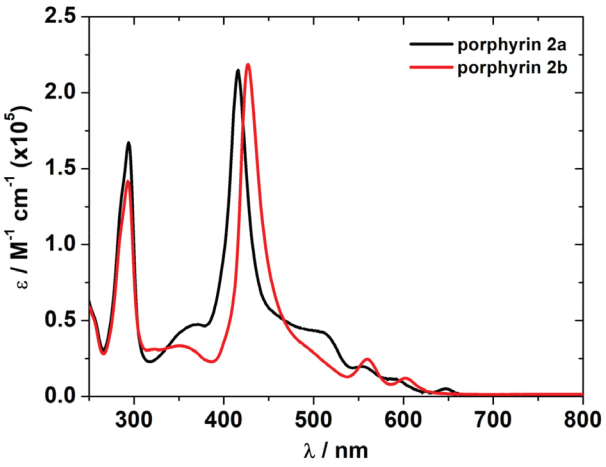

Figure 2. UV-Vis absorption spectra of 6.0-6.25 × 10^{-6} M porphyrins **2a** and **2b** solution in CH_3CN.

was detected at 294 nm ($\pi \rightarrow \pi^*$) in acetonitrile solution. In addition, the metal-to-ligand charge-transfer (MLCT) transition band ($Ru^{II}(d\pi \rightarrow$ bpy-$p\pi^*)$) was observed in the 470-490 nm range, but it is superimposed to the most intense porphyrin bands since its molar absorptivity is relatively low (Figure 2). In the case of zinc(II) porphyrin **2b**, the Soret band shifted to 427 nm and the typical four Q-bands profile in the visible range was converted in two bands at 559 and 603 nm (Figure 2). The absorption data and molar absorptivity values for the porphyrins under study are listed in Table 1.

Electrochemistry properties of tetra-ruthenated porphyrins

Typical cyclic voltammograms of the tetra-ruthenated porphyrin systems in dry DMF solution in the −1.50 to +1.50 V range, at scan rate of 50-200 mV s^{-1}, are shown in Figure 3. Porphyrin **2a** presents three reversible redox processes. At anodic region, a strong reversible wave appears at $E_{1/2}$ = +0.90 V, attributed to the Ru^{3+}/Ru^{2+} redox pair (Table 2). In the case of zinc-complex **2b**, the same oxidation process was observed at $E_{1/2}$ = +0.89 V, followed by an irreversible peak at E_{pa} = +1.43 V, which can be

Table 1. Absorption data for the porphyrin derivatives **1a**, **2a** and **2b**, in CH_3CN

Transition band	λmax (ε, molar absorption / (M^{-1} cm^{-1})) / nm		
	Porphyrin **1a**	Porphyrin **2a**	Porphyrin **2b**
Vinyl-Py	369 (22,595)	–	–
Soret	417 (303,175)	416 (214,425)	427 (218,580)
Q bands	512 (16,250), 546 (5,110), 587 (5,185), 643 (2,155)	512 (42,000), 555 (19,840), 592 (11,600), 647 (5,250)	560 (24,725), 602 (12,060)
$\pi \rightarrow \pi^*$	–	294 (167,000)	293 (141,510)
MLCT	–	ca. 485	ca. 497

MLCT: metal-to-ligand charge-transfer.

attributed to the mono-electronic oxidation of the porphyrin ring (see Figure S9, SI section). Also, it can be observed that the redox potentials did not change significantly when the scan rate was increased from 50 to 200 mV s^{-1} meaning that there is no limitation related to charge transfer kinetics and the redox reaction is controlled by diffusion process.

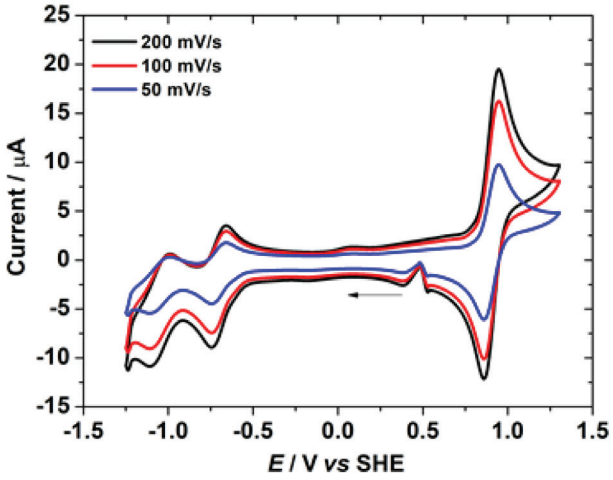

Figure 3. Cyclic voltammograms of free-base tetra-ruthenated porphyrin **2a**, in dry DMF solution with 0.1 M of $TBAClO_4$, at scan rate of 200 mV s^{-1} (black line), 100 mV s^{-1} (red line) and 50 mV s^{-1} (blue line).

Table 2. Redox potentials (*versus* SHE) of porphyrins in DMF solution

Porphyrin	$P^{-/2-}$ / V	$P^{0/-}$ / V	$P^{0/+}$ / V	$Ru^{3+/2+}$ / V
1a	−1.40[a]	−0.92[a]	+1.13[b]	–
2a	−1.05[c]	−0.70[c]	–	+0.90[a]
2b	−1.21[c]	−0.99[c]	+1.43[b]	+0.89[a]

[a]$E_{1/2}$ values; [b]anodic peak; [c]cathodic peak.

Moving to the cathodic region, the two reversible waves at −0.70 and −1.05 V can be assigned to the first and second mono-electronic reduction processes of the porphyrin ring, forming the porphyrin π-anion radical and π-dianion species (Figure 3; Table 2). No redox process could be assigned to the vinyl and bipyridine groups since they are in more negative potentials. The tetra-ruthenated zinc(II) porphyrin **2b** exhibits a similar electrochemical behavior, and all redox processes were confirmed by UV-Vis spectroelectrochemistry analysis as described below.

Spectroelectrochemistry analysis of tetra-ruthenated porphyrins

Spectroelectrochemical techniques are especially useful, providing direct evidence of the redox sites involved, as well as the electronic interactions in a multibridged system as a function of the several possible oxidations states.[19] In this case, the electronic UV-Vis spectrum of tetra-ruthenated porphyrin **2a** exhibited characteristic porphyrin absorption bands at 417 nm (Soret band), 512 to 647 nm range (Q bands), while the $[Ru^{II}(bpy)_2Cl]^+$ moieties exhibited bands at 294 nm (intraligand bpy transition; $\pi \rightarrow \pi^*$) and 485 nm (MLCT, Ru^{II}-to-bipy charge transfer envelope).

The oxidation of the tetra-Ru^{II} free-base porphyrin at +0.90 V was confirmed by applying potentials from 0 to +1.20 V, leading to the complete decay of the MLCT bands in the 480-490 nm region, splitting of the bpy $\pi \rightarrow \pi^*$ transition band at 294 nm into two peaks around 303 and 316 nm with lower intensity and inducing the bathochromic shift of the Soret band from 417 to 422 nm (Figure 4a).

Based on the intensity of the corresponding electrochemical waves and on the dramatic changes in the electronic bands associated with the $[Ru^{II}(bpy)_2Cl]^+$ moiety, the redox process observed at 0.90 V can be unequivocally ascribed to the Ru^{3+}/Ru^{2+} redox couple. The fact that the four $[Ru^{II}(bpy)_2Cl]^+$ groups were oxidized at the same potential is consistent with a weak coupling between the Ru^{3+}/Ru^{2+} redox pairs as previously observed for related polynuclear and polymeric systems. The reversibility of the Ru^{3+}/Ru^{2+} process is confirmed by scanning in the reverse direction, from +1.20 to 0 V, when the bpy $\pi \rightarrow \pi^*$ band as well as all initial spectral features are completely recovered (see Figure S10, SI section). In the case of zinc(II) porphyrin **2b**, the Ru^{3+}/Ru^{2+} redox couple process was observed at +0.89 V, whilst the porphyrin ring oxidation process took place around +1.45 V leading to a decay of the Soret and Q bands, with minor changes in the bpy $\pi \rightarrow \pi^*$ transition. A similar behavior was observed for the free-base porphyrin **2b** (Figure S11, SI section).

In the negative region between 0.00 and −1.50 V, the reduction processes of the porphyrin **2a** at −0.70 V leads to a systematic bathochromic shift of the Soret and Q bands to 449, 578 and 627 nm, with several simultaneous isosbestic points consistent with a well-behaved, reversible process involving the tetra-ruthenated porphyrin **2a**, as shown in Figure 4b. In this way, the first reduction process can be attributed to the characteristic π-anion radical species, followed by a second monoelectronic reduction process at −1.05 V, leading to a decay of the Soret and Q bands, as well as rise of new absorption bands at 525 and 785 nm, simultaneously with a decay of the $\pi \rightarrow \pi^*$ transition band at 294 nm, assigned to the formation of porphyrin dianion species and monoelectronic reduction of some bipy ligand (Figure 4c). Moreover, the spectral changes and redox profile were similar in the case of zinc(II) porphyrin compound **2b** (see Figure S12, SI section).

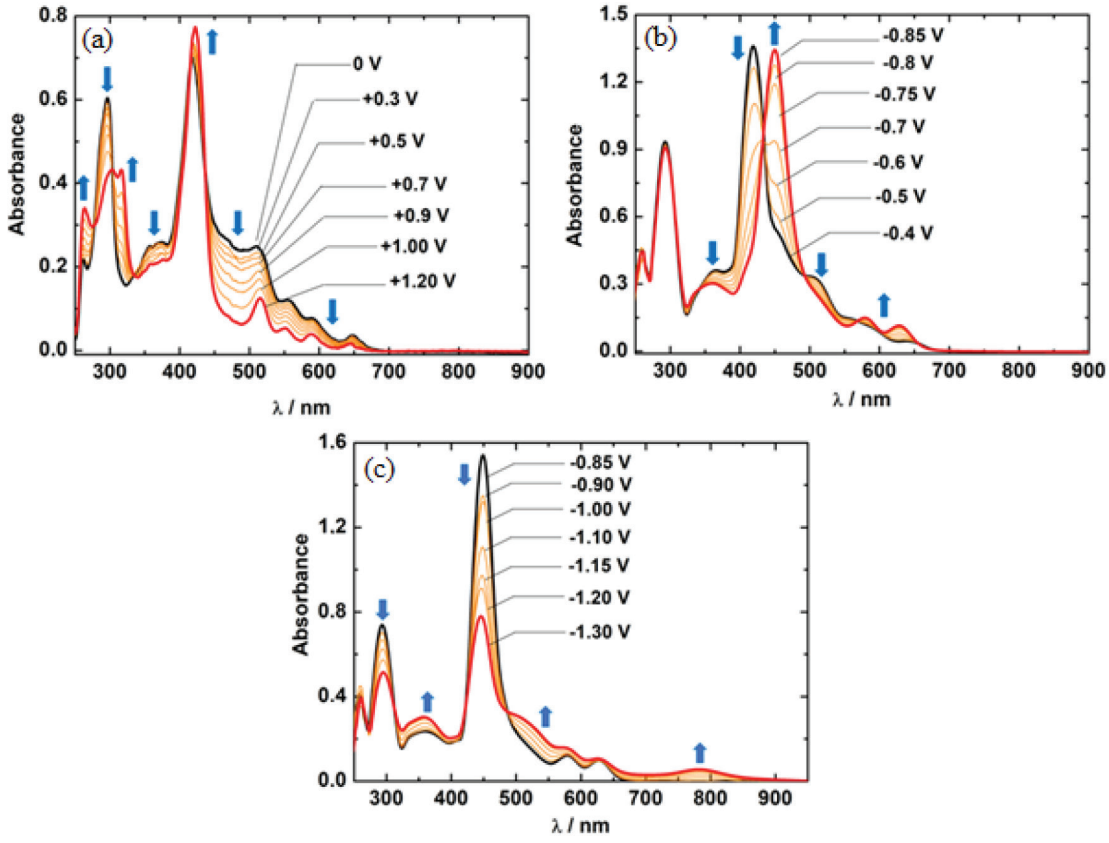

Figure 4. UV-Vis spectroelectrochemistry profile of porphyrin **2a**, in 0.1 mol L^{-1} $TBAClO_4$, in DMF from (a) 0.00 to +1.20 V; (b) –0.40 to –0.85 V; and (c) –0.85 to –1.30 V.

Electrochemical behavior of thin films of porphyrins **2a** and **2b**

Thin films of tetra-ruthenated porphyrins **2a** and **2b** were obtained by transferring a methanolic solution onto the surface of a glassy carbon electrode and letting it dry. Then, the electrochemical behavior of such porphyrin thin films was evaluated by cyclic voltammetry and electrochemical impedance spectroscopy (see Figures S9 and S13, SI section).

The cyclic voltammograms of electrodes modified with **2a** and **2b** in aqueous solution, in the absence and presence of increasing concentrations (from 9.9×10^{-5} to 1.1×10^{-3} mol L^{-1}) of nitrite substrate, are presented in the Figures 5a and 5b. In the +0.22 to +1.22 V potential range, the electrodes presented a pair of well-defined waves with E_{pa} = +1.01 V and E_{pc} = +0.95 V, and $E_{1/2}$ = +0.98 V, related to the Ru^{3+}/Ru^{2+} redox process. The oxidation of nitrite to nitrate on a conventional electrode is irreversible and presents a slow kinetics, requiring an overpotential to occur. However, the porphyrins **2a** and **2b** films can mediate such kind of electron-transfer reaction in aqueous solution when in the presence of reducing analytes. In the Figures 5a and 5b, it is possible to observe the increase of the anodic wave current intensity around ca. 1.02 V, when sodium nitrite was added into the solution. A good linear correlation was obtained from 9.9×10^{-5} to 1.1×10^{-3} mol L^{-1} for both electrodes, which can be fitted by the equations $i = 0.11$ [nitrite] + 1×10^{-4} A ($R^2 = 0.996$), where i is the current, and $i = 0.12$ [nitrite] + 5.65×10^{-5} A ($R^2 = 0.999$) for electrodes modified with **2a** and **2b**, respectively, as shown in the Figure 5c.

In order to better understand the electrochemical behavior of porphyrins **2a** and **2b**, electrochemical impedance spectroscopy experiments were performed and the respective Nyquist plots from 100 kHz to 0.1 Hz and Randle's circuit shown in the Figure 5d. It is possible to see that the electrodes modified with **2a** and **2b** showed a semicircle at high frequencies related to the charge transfer resistance (Rct), which in this case is referred to the Ru^{3+}/Ru^{2+} redox process. Those semicircles can be viewed in detail in the Figure 5d where it become clear that the electrode modified with compound **2b** has a smaller Rct than porphyrin **2a**, respectively 36.70 and 45.17 Ω. Also, the Randle's circuit obtained after fitting the Nyquist plots of electrodes modified with **2a** and **2b** is presented as inset of Figure 5d. The regions (1), (2) and (3), highlighted in the Randle's circuit, are related to the

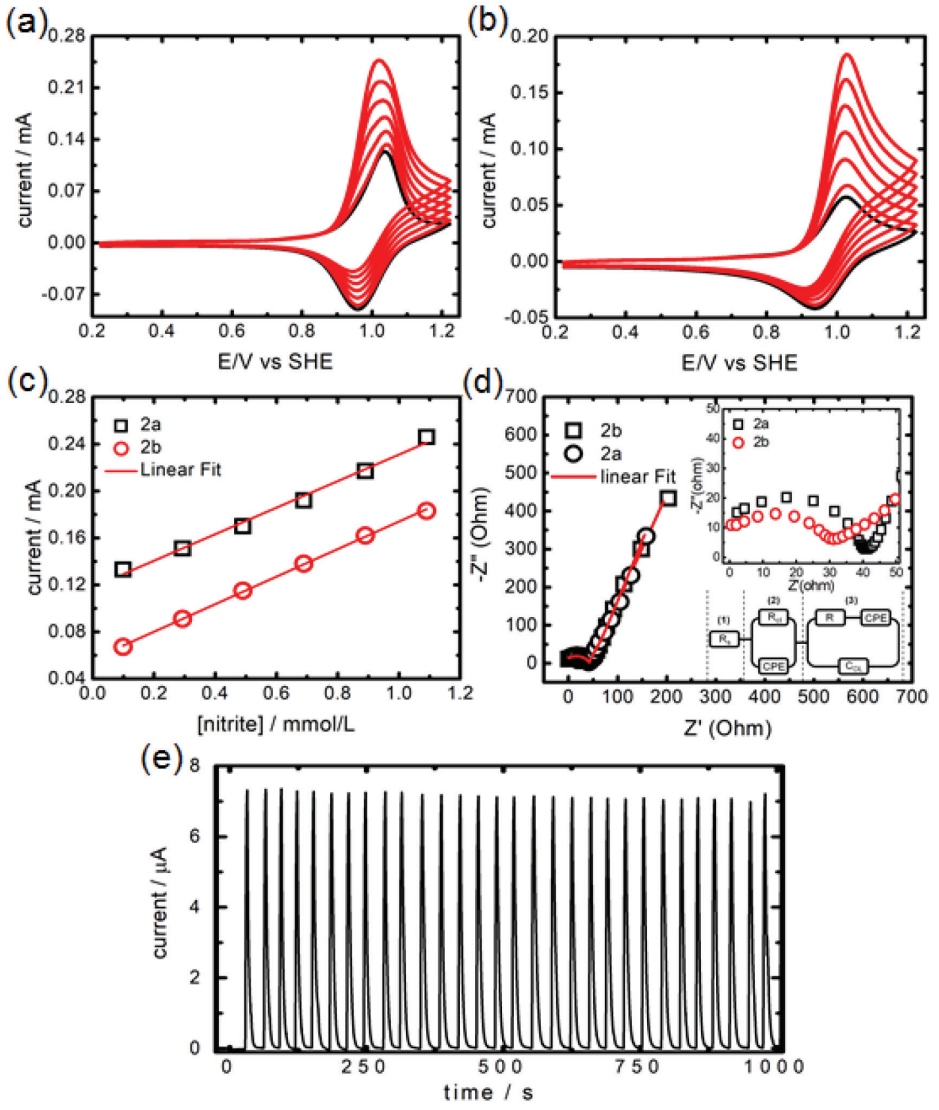

Figure 5. Cyclic voltammograms of electrodes modified with (a) **2a** and (b) **2b** in the absence (black line) and presence (red line) of increasing nitrite concentrations in the 9.9×10^{-5} to 1.1×10^{-3} mol L^{-1} range; the respective (c) current *vs*. nitrite concentration, and (d) Nyquist plots; (e) FIAgram showing a set of 30 consecutive injections of nitrite solution (1.0×10^{-4} mol L^{-1}) using a flow rate of 1.0 mL min^{-1} and a potential of +1.10 V *vs*. SHE. Inset of (d): expanded view of Nyquist plots at high frequencies and corresponding Randle's equivalent circuit used for modelling.

solution resistance, charge transfer resistance and diffusion process, respectively.

As the zinc(II) derivative **2b** presented better results (based on sensitivity and Rct data, respectively, from CV and EIS) than the electrodes modified with free-base porphyrin **2a**, the analytical repeatability of **2b** was chosen to be evaluated under hydrodynamic conditions in a FIA system. Figure 5e shows the amperometric FIAgram of 30 sucessive injections of 100 µL of nitrite solution (1.0×10^{-4} mol L^{-1}) using a flow rate of 1.0 mL min^{-1} and a potential of +1.20 V *vs*. SHE. The average signal was of 6.97 ± 0.094 µA) and relative standard deviation (RSD, n = 30) of 1.36% suggesting that the modified electrode presents an excellent response even under hydrodynamic conditions, sustaining a stable current signal. Thus, these results lead us to believe that the material is not being leached out from the electrode surface into the solution, demonstrating the great potential of porphyrin **2b** as amperometric sensor for nitrite.

Aggregation studies by UV-Vis analysis

The evaluation of the aggregation behavior of porphyrins **2a** and **2b** in acetonitrile solution was studied by electronic UV-Vis absorption spectroscopy.[40] In general, tetrapyrrolic macrocycles with bulky moieties sticking out from the ring plane are prevented from π-stacking interactions, avoiding aggregation in solution.[41] No significant shift at the maximum absorbance wavelength was observed in all cases. A linear increase was observed

in the UV-Vis absorption spectrum as a function of the concentration in the 0.1 to 5.0 μM range (as shown for porphyrin **2a** in Figure S14, SI section). The spectroscopic results indicated that the aggregation process is not significant in any of the porphyrin under study (see the aggregation behavior of zinc(II) complex **2b** spectra in DMSO in the Figure S14, SI section).

Photostability and singlet oxygen generation ($^1O_2$) experiments

Photosensitizers (PS) must be stable under light irradiation for long periods of time to be efficient. Thus, photostability evaluation is an important parameter considering application in photodynamic therapy since the photogenerated singlet oxygen (see below) can react with the PS promoting its own degradation.[42] From the small changes on the absorbance spectrum as a function of the time, it was confirmed that tetra-ruthenated porphyrins **2a** and **2b** present good stability under white-LED radiation (fluence rate 25 mW cm^{-2} and light dosage 90 J cm^{-2}) in the range of 400-800 nm during 60 min in DMSO solution (see Figure S15, SI section).

The ability of Ru^{II}-porphyrins **2a** and **2b** to produce singlet oxygen species was determined in DMF solution using a chemical method based on DPBF.[25] The porphyrin derivative **1a** (without ruthenium(II)-moiety) was used as reference. Porphyrins **1a**, **2a** and **2b** at a concentration of 0.5 μM were able to photo-oxidize DPBF at a concentration of 20 μM (Figure 6). Porphyrins **2a** and **2b** (with $[Ru(bpy)_2Cl]^+$ units and zinc(II) ion, respectively) were moderate generators of singlet oxygen species decomposing 20.0 and 25.0% of DPBF, respectively, after 180 s irradiation with a red diode laser source (λ = 660 nm, 100 mW). Both Ru^{II}-derivatives have a similar photo-oxidation effect on DPBF when compared to the corresponding reference **1a** (23.0%). The ability of these studied porphyrins to photo-oxidize DPBF decreased in the sequence **2b** > **1a** > **2a**. The relatively low singlet oxygen production may be attributed to the formation of other reactive oxygen species (such as hydroxyl and superoxide radical species) that are not determined by this type of experiment. The great photostability and ability of porphyrins **1a**, **2a** and **2b** under light irradiation to generate $^1O_2$ allowed us to envisage them as potential sensitizers in photodynamic therapy (PDT) applications.

The ability of porphyrins **1a**, **2a** and **2b** to produce $^1O_2$ was monitored using DPBF in DMSO. The DPBF method has been widely used to provide a quantitative analysis of singlet oxygen production since the reaction product (1,2-dibenzoylbenzene) does not absorb visible light. It is a popular measurement procedure because of its simplicity in evaluating $^1O_2$ generated by type II photo processes.[43] In this procedure, changes on the DPBF absorbance are directly proportional to the amount of singlet oxygen generated. In this study, the photo-degradation rate constants (k) and singlet oxygen quantum yield of porphyrins **1a**, **2a** and **2b** was determined, and the values are presented in Table 3. Some typical set of spectra monitoring the kinetics of DPBF photo-oxidation are shown in the SI section (see Figures S16-S18).

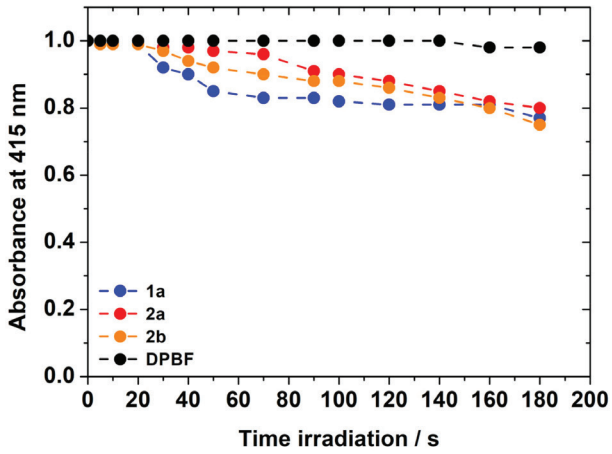

Figure 6. Photo-oxidation of DPBF (20 μM) in DMF with or without porphyrin derivatives **1a**, **2a** and **2b** at a concentration of 0.5 μM, after red-light irradiation (660 nm) at 100 mW. The DPBF absorbance was recorded at 415 nm.

Table 3. Photo-degradation rate constants and singlet oxygen quantum yields of porphyrins **1a**, **2a** and **2b** in DMSO solution

Porphyrin	k / min^{-1}	Φ_Δ (DMSO)
1a	0.0044	0.37
2a	0.0015	0.14
2b	0.0030	0.27
TPP[a]	0.0084	0.66

[a]As standard in DMF solution. k: photo-degradation kinetic rate constant; Φ_Δ: singlet oxygen production quantum yield; DMSO: dimethyl sulfoxide; TPP: *meso*-tetra(phenyl)porphyrin.

The singlet oxygen quantum yields from 0.14 to 0.37 were measured for the porphyrins in DMSO solution, values lower than for the TPP standard (Φ_Δ^{std} = 0.66), and in a different sequence as compared with that found previously in DMF solution, probably reflecting some solvent effect. Also, considering that the free-base **1a** derivative exhibits a quantum yield that is more than twice as large than that of **2a**, a significant excited state quenching by the peripheral $[Ru(bpy)_2Cl]^+$ seems to be taking place. However, such effect is minimized in the zinc(II) derivative **2b** suggesting a redox mechanism involving an electron transfer from

the ruthenium complex to the free-base porphyrin ring. The ability to generate $^1O_2$ upon exposure to light in the presence of oxygen allowed us to envisage those porphyrins as potential photo-cleavage agents in photo-oxidative processes.

Fluorescence emission studies for the porphyrins **1a**, **2a** and **2b**

The *meso*-tetra(4-pyridylvinylphenyl)porphyrin **1a** in argon-saturated acetonitrile solution exhibits fluorescence emission in the 600 to 800 nm range, corresponding to the typical $S_1 \rightarrow S_0$ and $S_2 \rightarrow S_0$ transitions (Figure 7), when excited in the Soret band. When porphyrin **1a** is coordinated with $[Ru(bpy)_2Cl]^+$ units in the peripheral pyridyl groups, the emission spectral profile remained characteristic of the porphyrin macrocycle. In this way, the luminescence state was expected to be centered on the lowest singlet excited state, S_1, of the porphyrin and not on the lowest excited triplet state of the ruthenium(II) complexes.[44] In these experiments, TPP was used as standard and the fluorescence emission data were listed in Table 4.

The observed fluorescence emission behavior may be explained by the specific interactions of pyridyl groups

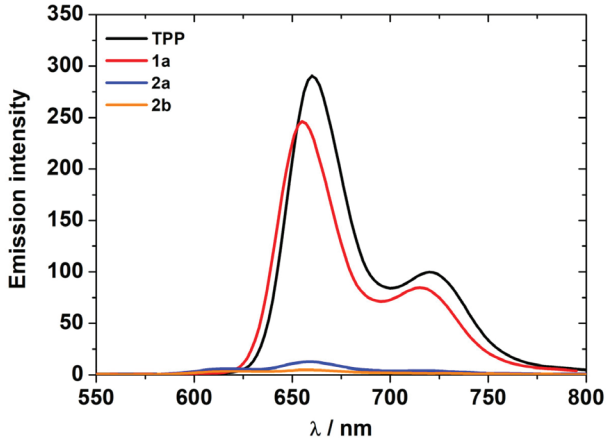

Figure 7. Steady-state fluorescence emission spectra (λ_{exc} = Soret band) of the porphyrins **1a**, **2a** and **2b**, in argon-saturated acetonitrile solution.

Table 4. Fluorescence quantum yield (Φ_F) of the porphyrins **1a**, **2a** and **2b** in argon-saturated CH_3CN solution (λ_{exc} = Soret band), at room temperature

Porphyrin	Φ_F (Soret band) / %	Emission band / nm
TPP[a]	13.0	660, 721
1a	10.0	655, 715
2a	7.0	620, 656
2b	4.0	625, 657

[a]In DMSO solution.[45] TPP: *meso*-tetra(phenyl)porphyrin.

with the solvent molecules through the nitrogen atom lone pair, and also non-specific dipole-dipole interactions. Those interactions should be improving the vibronic coupling with the solvent molecules increasing the excited state non-radioactive decay rate to the ground state.

The fluorescence quantum yield of the porphyrins indicates the capacity of an excited molecule (in the first excited state) to return to the electronic ground state by photon emission.[21] This process depends on the electronic structure as well as solvent effects, in addition to steric and conformational interactions. In this case, fluorescence quantum yields were determined at an optical density (OD) in the range of 0.01 to 0.03. By inserting the $[Ru(bpy)_2Cl]^+$ peripheral complexes at the *para*-position of the pyridyl groups, the fluorescence quantum yield decreased when compared to the TPP standard and porphyrin **1a**. This fact may be explained by the presence of electrochemically active Ru^{II}-complexes (redox quencher) at the *meso*-pyridyl positions that also can interact through the heavy atoms effect.[31,46] In fact, the spin-orbit coupling factor of the ruthenium(II) complexes can increase the rate of non-radiative decay pathways and eventually decrease the contribution of the radiative decay pathways.[35,47,48]

Biomolecule interactive studies

HSA-binding properties

The fluorescence emission from HSA is usually obtained exciting the protein at λ_{exc} = 290 nm due to the high contribution of tryptophan residues (Trp-214). As example, Figure 8 shows the fluorescence emission spectra of HSA without and in the presence of successive additions of free-base tetra-ruthenated porphyrin **2a** and **2b**. The HSA spectra for the association with porphyrin **1a** are depicted in Figure S19 of the SI section. The albumin solution presents a strong fluorescence emission peak around 335 nm and the quenching of this fluorescence peak can be used to investigate the interaction of albumin with the porphyrins.

In this experiment, the fluorescence emission intensity of HSA decreased gradually upon increasing the concentrations of porphyrin in the protein solution indicating that the tetrapyrrolic macrocycle derivatives interacts with the protein (Figure 8). The quenching of the albumin fluorescence can be induced by different mechanisms,[49] which are in general classified in dynamic, static or combined quenching mechanisms. The nature of the fluorescence quenching mechanism induced by the porphyrins **1a**, **2a** and **2b**, was examined using the well-known Stern-Volmer equation 3 (see Experimental section). The results have shown a good linear relationship and the quenching constants (K_{SV} and k_q) at room temperature (298 K) were calculated for the

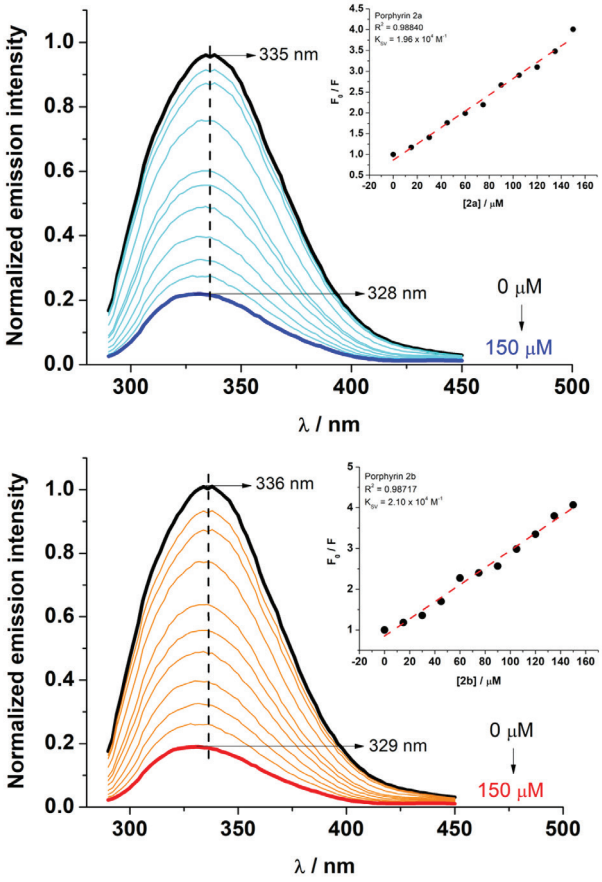

Figure 8. The HSA fluorescence emission spectra without and as a function of porphyrin **2a** (top) and **2b** concentration (bottom), in a Tris-HCl buffer (pH = 7.4). The concentration of HSA is 10 μM and porphyrin concentrations ranged from 0 to 150 μM. Inset: plot of F_0/F *versus* [porphyrin].

HSA-porphyrin adducts. The results shown in Table 5 clearly indicate that the quenching occurs by static collision quenching mechanism (k_q higher than k_{diff}) upon association of HSA with a porphyrin in the ground state.[50]

The association constant K_a and the number of binding sites (n) were calculated using the double logarithmic approximation (equation 4, see Experimental section). The number of the binding sites for each porphyrin and HSA was observed in the range between 1.31 and 1.88. Since the n values are variable, the porphyrin derivatives probably are interacting with different binding sites of HSA, or by different modes, where can occupy more than one subdomain at the same time, mainly due to the large volume of the porphyrin molecules under study. In addition, the K_a values determined by the fluorescence quenching experiments showed a good correlation with the K_{SV} values (both constants are in the same order of magnitude for a given compound), suggesting that the porphyrins can interact with HSA, but present weak binding ability.[51] Moreover, The thermodynamic analysis via ΔG° values (−4.9 to −6.70 kcal mol^{-1} range), indicated that all porphyrins tend to form a more or less stable adduct with HSA, especially the tetra-ruthenated porphyrins presenting $[Ru^{II}(bpy)_2Cl]^+$ moieties (**2a** and **2b**).

Molecular docking analysis for the HSA-poprhyrin interaction

The HSA structure presents three main binding sites which are located in the IIA, IIIA and IB subdomains. Generally, small aromatic organic compounds with carbonyl, carboxyl and hydroxyl groups bind to the IIA subdomain (site I), for example, warfarin, acenocoumarin and oxyphenylbutazone, while small organic acid compounds bind to the IIIA subdomain (site II), e.g., ibuprofen, flurbiprofen and flufenamic acid.[52] Subdomain IB (site III) has been identified as potential site for interaction of high volume compounds, e.g., digitoxin and porphyrins.[8,30] In order to identify the main binding site for the porphyrins **1a**, **2a** and **2b**, as well as to offer an atomic level explanation on the interaction mode (the main amino acid residues and intermolecular forces which contribute to the binding process), molecular docking calculations were carried out. Table 6 shows the highest docking score value (more positive the value stronger the interaction) for the HSA:porphyrin interactions in the three main binding sites. All were favorable to the interaction (positive score values), however, site III presented the most positive value, being an indication that the porphyrins will interact preferentially with the IB subdomain. From literature, protoporphyrin IX[40] and *meso*-tetra-(4-pyridyl)porphyrins with ruthenium(II) bipyridiyl peripheral complexes[41] bind preferentially to site III, in agreement with the presented results.

Table 5. The human serum albumin (HSA)-porphyrin **1a**, **2a** and **2b** binding parameters

Porphyrin	Q[a] / %	K_{SV}[b] / M^{-1}	k_q[c] / (M^{-1} s^{-1})	K_a[d] / M^{-1}	n[e]	ΔG°[f] / (kcal mol^{-1})
1a	29.0	2.52×10^3	4.44×10^{11}	4.54×10^3	1.31	−4.98
2a	77.4	1.96×10^4	3.46×10^{12}	7.66×10^4	1.88	−6.66
2b	81.4	2.10×10^4	3.70×10^{12}	6.78×10^4	1.65	−6.59

[a]Quencher: $Q(\%) = (Emission_{initial} - Emission_{final}) / (Emission_{initial}) \times 100$; [b]Stern-Volmer quenching constant; [c]bimolecular quenching rate constant determined by steady-state fluorescence emission spectra (τ_0 HSA = 5.67×10^{-9} s); [d]association equilibrium constant of porphyrin with HSA determined by steady-state emission spectra; [e]number of binding sites; [f]free-energy value obtained using T = 298 K and R = 1.987 kcal K^{-1} mol^{-1}.

Table 6. Molecular docking score values for the interaction of human serum albumin (HSA) with porphyrins **1a**, **2a** and **2b**

Porphyrin	Site I	Site II	Site III
1a	61.5	38.5	79.5
2a	58.5	33.5	65.8
2b	55.5	30.9	60.3

Molecular docking results suggested hydrogen bonding and van der Waals forces as the main intermolecular interactions between the amino acid residues at IB subdomain and the porphyrins structure. Figure 9 and Table 7 show the best docking conformation and the main amino acid residues which interact with porphyrins in the subdomain IB of HSA protein (the main binding

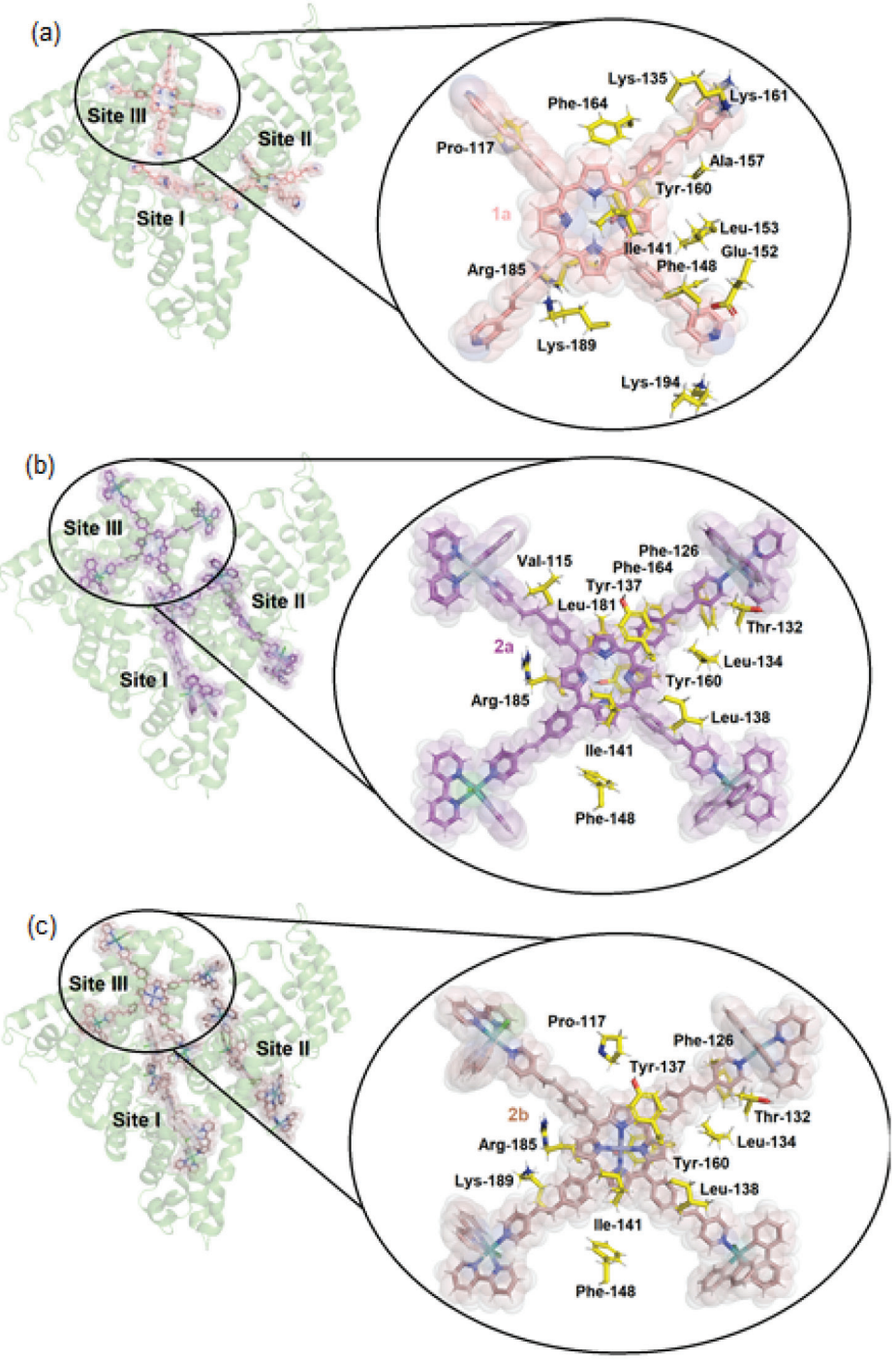

Figure 9. Superposition of the best docking pose for the three main binding pockets and the main amino acid residues which can interact with (a) HSA:**1a**; (b) HSA:**2a** and (c) HSA:**2b** in the subdomain IB (site III). Selected amino acid residues, porphyrins **1a**, **2a** and **2b** are represented as yellow, beige, orange, and purple sticks, respectively. Elements' color code: hydrogen: white; oxygen: red; nitrogen: dark blue; chloro: green; Zn^{II}: gray; Ru^{II}: dark green.

Table 7. Molecular docking results for the interaction between HSA:porphrins in the site III

Porphyrin	Amino acid residue	Interaction	Distance / Å
1a	Pro-117	van der Waals	1.30
	Lys-135	hydrogen bonding	2.30
	Ile-141	van der Waals	3.80
	Phe-148	van der Waals	2.60
	Glu-152	van der Waals	2.20
	Leu-153	van der Waals	3.40
	Ala-157	van der Waals	2.60
	Tyr-160	hydrogen bonding	2.20
	Lys-161	hydrogen bonding	2.80
	Phe-164	van der Waals	3.50
	Arg-185	van der Waals	2.50
	Lys-189	van der Waals	2.60
	Lys-194	van der Waals	3.50
2a	Val-115	van der Waals	2.30
	Phe-126	van der Waals	3.60
	Thr-132	van der Waals	2.40
	Leu-134	van der Waals	3.60
	Tyr-137	van der Waals	1.90
	Leu-138	van der Waals	1.00
	Ile-141	van der Waals	3.10
	Phe-148	van der Waals	3.10
	Tyr-160	hydrogen bonding	3.60
	Phe-164	van der Waals	3.70
	Leu-181	van der Waals	3.50
	Arg-185	van der Waals	2.50
2b	Pro-117	van der Waals	3.10
	Phe-126	van der Waals	3.50
	Thr-132	van der Waals	2.60
	Leu-134	van der Waals	2.40
	Tyr-137	van der Waals	2.70
	Leu-138	van der Waals	3.60
	Ile-141	van der Waals	3.10
	Phe-148	van der Waals	2.30
	Tyr-160	hydrogen bonding	2.20
	Arg-185	van der Waals	2.60
	Lys-189	van der Waals	1.60

Pro: proline; Ile: isoleucine; Phe: phenylalanine; Glu: glutamine; Leu: leucine; Ala: alanine; Arg: arginine; Lys: lysine; Tyr: tryptophan; Val: valine.

pocket previously described above is site III). As example, the hydrogen from –NH group of lysine (Lys-135 and Lys-161) residues is a potential hydrogen bonding site with the lone pair electrons of the pyridine nitrogen atoms of free-base porphyrin **1a**, within a distance of 2.30 and 2.80 Å, respectively, while the acidic hydrogen of tyrosine (Tyr-160) residue –OH group also interact via hydrogen bonding but with the inner ring nitrogen atoms of porphyrin **1a** tetrapyrrolic macrocycle, within a distance of 2.20 Å. On the other hand, van der Waals forces were also identified between proline (Pro-117), isoleucine (Ile-141), phenylalanine (Phe-148 and Phe-164), glutamine (Glu-152), leucine (Leu-153), alanine (Ala-157), arginine (Arg-185), lysine (Lys-189 and Lys-194) residues and porphyrin **1a** molecule, within a distance of 1.30, 3.80, 2.60, 2.20, 3.40, 2.60, 3.50, 2.50, 2.60, and 3.50 Å, respectively. Overall, the coordination of Zn^{II} ion to the ring and ruthenium(II)-bpy complexes to the peripheral pyridyl groups of porphyrin **1a** decreased the ability of the porphyrin to interact via hydrogen bonding and increased the van der Waals interactions. In addition, molecular docking results indicated that porphyrins **2a** and **2b** present moieties that can occupy another subdomain than those occupied by the porphyrin core (Figure 9), being in good agreement with the experimental number of binding sites described above.

Conclusions

In summary, we described an useful and convenient route for preparation of a novel free-base *meso*-tetra(4-pyridylvinylphenyl)porphyrin (**1a**) and its functionalization with $[Ru(bpy)_2Cl]^+$ units, to form the *meso*-tetra-ruthenated(4-pyridylvinylphenyl)porphyrin (**2a**) and its respective zinc(II) complex (**2b**). The 4-vynilphenyl bridge increases the distance of the porphyrin ring and the ruthenium complexes thus decreasing the electronic coupling and the electrostatic interaction in between the positively charged ruthenium complexes, while increasing the possibilities of their interaction with biomolecules. As expected, the redox and spectroelectrochemical properties were similar to that observed for the analogous tetra(4-pyridyl)porphyrin derivatives, in addition to generating stable electrocatalytic active tetra-ruthenated porphyrins **2a**-**2b** modified electrodes exhibiting great potential as amperometric sensor for nitrite analysis. But the photophysical and singlet oxygen production was somewhat surprising since showed very low fluorescence quantum yields but moderate production of singlet oxygen and quite strong interactions with HSA in the ground state, which may be relevant for photodynamic therapy application. The longer and more spread apart arms (branches) with ruthenium polypyridyl complex at the end seems to activate an interaction mode involving the subdomain IB and other interaction site that may play relevant role in PDT.

Supplementary Information

Supplementary data (ESI-MS spectrum of porphyrin **1a** in the positive mode; UV-Vis spectrum of porphyrin **1a**; ^{1}H NMR spectrum of porphyrins **1a**, **2a** and **2b**; cyclic voltammogram of free-base porphyrin **1a**; ^{1}H-^{1}H COSY 2D spectrum of porphyrins **2a** and **2b**; cyclic voltammogram of free-base tetra-ruthenated porphyrin **2b**; UV-Vis spectroelectrochemistry profile of porphyrins **2a** and **2b**; FIA scheme for nitrite determination; aggregation study of the porphyrins **2a** and **2b** in DMSO solution; photostability plot of porphyrin derivatives **2a** and **2b**; photodegradation of DPBF by irradiation with diode laser in the presence of porphyrins **1a**, **2a** and **2b**; HSA fluorescence emission spectra without and in the presence of porphyrin **1a**; computational details for the molecular docking simulations of the porphyrins **1a**, **2a**, and **2b**) are all available free of charge at http://jbcs.sbq.org.br as PDF file.

Acknowledgments

The authors gratefully acknowledge the financial support from Conselho Nacional de Desenvolvimento Científico e Tecnológico (CNPq), Coordenação de Aperfeiçoamento de Pessoal de Nível Superior (CAPES) and Fundação de Amparo à Pesquisa do Estado de São Paulo (FAPESP). Paulo R. Martins acknowledges CNPq for the grant 408222/2016-6. Bernardo A. Iglesias thanks to Conselho Nacional de Desenvolvimento Científico e Tecnológico (CNPq, Universal Grant 409150/2018-5 and PQ Grants 304711/2018-7) and CAPES/PROEX, finance code 001. Koiti Araki acknowledges FAPESP (2018/21489-1) and CNPq (401581/2016-0 and 303137/2016-9) for the financial support.

Author Contributions

Viviane Viecelli synthesized and characterized porphyrins and wrote the first draft of the paper; Otávio A. Chaves contributed with molecular docking calculation structures and to manuscript writing; Koiti Araki contributed with financial structure for the development of the experiments and wrote the final version of the paper; Paulo R. Martins contributed with electrochemical analysis and to manuscript writing; Bernardo A. Iglesias contributed with laboratory, financial structure for the development of the experiments and wrote the final version of the paper.

References

1. Makarska-Bialokoz, M.; *Spectrochim. Acta, Part A* **2018**, *200*, 263.
2. Mari, C.; Pierroz, V.; Ferrari, S.; Gasser, G.; *Chem. Sci.* **2015**, *6*, 2660.
3. Toma, H. E.; Araki, K.; *Coord. Chem. Rev.* **2000**, *196*, 307.
4. Almeida-Marrero, V.; van de Winckel, E.; Anaya-Plaza, E.; Torres, T.; de la Escosura, A.; *Chem. Soc. Rev.* **2018**, *47*, 7369.
5. Mayer, I.; Toma, H. E.; Araki, K.; *J. Electroanal. Chem.* **2006**, *590*, 111.
6. Barbosa, M. I. F.; Parra, G. G.; Correa, R. S.; Sampaio, R. N.; Magno, L. N.; Silva, R. C.; Doriguetto, A. C.; Ellena, J.; Barbosa Neto, N. M.; Batista, A. A.; Gonçalves, P. J.; *J. Photochem. Photobiol., A* **2017**, *338*, 152.
7. Toma, H. E.; Araki, K.; *Progress in Inorganic Chemistry*, vol. 56; Karlin, K. D., ed.; John Wiley & Sons Inc.: Hoboken, NJ, USA, 2009, p. 379.
8. Chaves, O. A.; Menezes, L. B.; Iglesias, B. A.; *J. Mol. Liq.* **2019**, *294*, 111581.
9. Araki, K.; Losco, P.; Engelmann, F. M.; Winnischofer, H.; Toma, H. E.; *J. Photochem. Photobiol., A* **2001**, *142*, 25.
10. Martins, P. R.; Popolim, W. D.; Nagato, L. A. F.; Takemoto, E.; Araki, K.; Toma, H. E.; Angnes, L.; Penteado, M. V. C.; *Food Chem.* **2011**, *127*, 249.
11. Ferreira, L. M. C.; Martins, P. R.; Araki, K.; Toma, H. E.; Angnes, L.; *Electroanalysis* **2015**, *27*, 2322.
12. Ferreira, L. M. C.; Martins, P. R.; Araki, K.; Angnes, L.; *Electroanalysis* **2019**, *31*, 688.
13. Bhyrappa, P.; Arunkumar, C.; Varghese, B.; *J. Porphyrins Phthalocyanines* **2007**, *11*, 795.
14. Osuka, A.; Fujikane, D.; Shinmori, H.; Kobatake, S.; Irie, M.; *J. Org. Chem.* **2001**, *66*, 3913.
15. Sun, J.-K.; Li, W.; Chen, C.; Ren, C.-X.; Pan, D.-M.; Zhang, J.; *Angew. Chem., Int. Ed.* **2013**, *52*, 6653.
16. Peters, T.; *All About Albumin: Biochemistry, Genetics, and Medical Applications*; Academic Press: San Diego, 1996.
17. Carter, D. C.; Ho, J. X.; *Adv. Protein Chem.* **1994**, *45*, 153.
18. Hu, J.; Allen, R.; Rozinek, S.; Brancaleon, L.; *Photochem. Photobiol. Sci.* **2017**, *16*, 694.
19. Strozik, T.; Wolszczak, M.; Hilczer, M.; *Radiat. Phys. Chem.* **2013**, *91*, 156.
20. Chaves, O. A.; Acunha, T. V.; Iglesias, B. A.; Jesus, C. S. H.; Serpa, C.; *J. Mol. Liq.* **2020**, *301*, 112466.
21. Geselowitz, D. A.; Kutner, W.; Meyer, T. J.; *Inorg. Chem.* **1986**, *25*, 2015.
22. Gomes, M. C.; Silva, S.; Faustino, M. A. F.; Neves, M. G. P. M. S.; Almeida, A.; Cavaleiro, J. A. S.; Tomé, J. P. C.; Cunha, Â.; *Photochem. Photobiol. Sci.* **2013**, *12*, 262.
23. Toma, H. E.; Araki, K.; *Curr. Org. Chem.* **2002**, *6*, 21.

24. Silva, S.; Pereira, P. M. R.; Silva, P.; Paz, F. A. A.; Faustino, M. A. F.; Cavaleiro, J. A. S.; Tomé, J. P. C.; *Chem. Commun.* **2012**, *48*, 3608.
25. Pivetta, R. C.; Auras, B. L.; de Souza, B.; Neves, A.; Nunes, F. S.; Cocca, L. H. Z.; de Boni, L.; Iglesias, B. A.; *J. Photochem. Photobiol., A* **2017**, *332*, 306.
26. Pineiro, M.; Carvalho, A. L.; Pereira, M. M.; Gonsalves, A. M. d'A. R.; Arnaut, L. G.; Formosinho, S. J.; *Chem. - Eur. J.* **1998**, *4*, 2299.
27. Foletto, P.; Correa, F.; Dornelles, L.; Iglesias, B. A.; da Silveira, C. H.; Nogara, P. A.; da Rocha, J. B. T.; Faustino, M. A. F.; Rodrigues, O. E. D.; *Molecules* **2018**, *23*, 2588.
28. Lakowicz, J. R.; *Principles of Fluorescence Spectroscopy*; Springer: New York, 2006.
29. Montalti, M.; Credi, A.; Prodi, L.; Gandolfi, M. T.; *Handbook of Photochemistry*; CRC Press Taylor & Francis: Boca Raton, 2006.
30. Wardell, M.; Wang, Z.; Ho, J. X.; Robert, J.; Ruker, F.; Ruble, J.; Carter, D. C.; *Biochem. Biophys. Res. Commun.* **2002**, *291*, 813.
31. *Spartan'14*; Wavefunction Inc., Irvine, USA, 2014.
32. http://www.ccdc.cam.ac.uk/solutions/csd-discovery/components/gold/, accessed in April 2020.
33. Ghuman, J.; Zunszain, P. A.; Petitpas, I.; Bhattacharya, A. A.; Otagiri, M.; Curry, S.; *J. Mol. Biol.* **2005**, *38*, 353.
34. Wang, Z. M.; Ho, J. X.; Ruble, J. R.; Rose, J.; Ruker, F.; Ellenburg, M.; Murphy, R.; Click, J.; Soistman, E.; Wilkerson, L.; Carter, D. C.; *Biochim. Biophys. Acta* **2013**, *1830*, 5356.
35. DeLano, W. L.; *PyMOL User's Guide*; DeLano Scientific LLC: San Carlos, CA, USA, 2002.
36. Adler, A. D.; Longo, F. R.; Shergalis, W.; *J. Am. Chem. Soc.* **1964**, *86*, 3145.
37. Iglesias, B. A.; Barata, J. F. B.; Pereira, P. M. R.; Girão, H.; Fernandes, R.; Tomé, J. P. C.; Neves, M. G. P. M. S.; Cavaleiro, J. A. S.; *J. Inorg. Biochem.* **2015**, *153*, 32.
38. Engelmann, F. M.; Losco, P.; Winnischofer, H.; Araki, K.; Toma, H. E.; *J. Porphyrins Phthalocyanines* **2002**, *6*, 33.
39. Musetti, C.; Spagnul, C.; Mion, G.; Da Ros, S.; Gianferrara, T.; Sissi, C.; *ChemPlusChem* **2015**, *80*, 158.
40. da Silveira, C. H.; Garoforo, E. N.; Chaves, O. A.; Gonçalves, P. F. B.; Streit, L.; Iglesias, B. A.; *Inorg. Chim. Acta* **2018**, *482*, 542.
41. Uchoa, A. F.; de Oliveira, K. T.; Baptista, M. S.; Bortoluzzi, A. J.; Iamamoto, Y.; Serra, O. A.; *J. Org. Chem.* **2011**, *76*, 8824.
42. Menezes, P. F. C.; Melo, C. A. S.; Bagnato, V. S.; Imasato, H.; Perussi, J. R.; *Laser Phys.* **2005**, *15*, 435.
43. Zhang, X. F.; Li, X.; *J. Lumin.* **2011**, *131*, 2263.
44. Gonçalves, P. J.; Bezzerra, F. C.; Menezes, L. B.; Teles, A. V.; Alves, K. M.; Alonso, L.; Alonso, A.; Andrade, M. A.; Borissevitch, I. E.; de Souza, G. R. L.; Iglesias, B. A.; *J. Photochem. Photobiol., A* **2020**, *391*, 112375.
45. Cocca, L. H. Z.; Gotardo, F.; Sciuti, L. F.; Acunha, T. V.; Iglesias, B. A.; de Boni, L.; *Chem. Phys. Lett.* **2018**, *708*, 1.
46. Azenha, E. G.; Serra, A. C.; Pineiro, M.; Pereira, M. M.; Melo, J. S.; Arnaut, L. G.; Formosinho, S. J.; Gonsalves, A. M. R.; *Chem. Phys.* **2002**, *280*, 177.
47. Monteiro, C. J. P.; Pina, J.; Pereira, M. M.; Arnaut, L. G.; *Photochem. Photobiol. Sci.* **2012**, *11*, 1233.
48. da Silva, A. R.; Pelegrino, A. C.; Tedesco, A. C.; Jorge, R. A.; *J. Braz. Chem. Soc.* **2008**, *19*, 491.
49. Kalanur, S. S.; Seetharamappa, J.; Kalalbandi, V. K. A.; *J. Pharm. Biomed.* **2010**, *53*, 660.
50. An, W.; Jiao, Y.; Dong, C.; Yang, C.; Inoue, Y.; Shuang, S.; *Dyes Pigm.* **2009**, *81*, 1.
51. Naveenraj, S.; Anandan, S.; *J. Photochem. Photobiol., C* **2013**, *14*, 53.
52. Sudlow, G.; Birkett, D. J.; Wade, D. N.; *Mol. Pharmacol.* **1976**, *12*, 1052.

Submitted: January 8, 2020
Published online: April 30, 2020